APL Materials

Cathodoluminescence and x-ray photoelectron spectroscopy of ScN: Dopant, defects, and band structure

Cite as: APL Mater. **8**, 081103 (2020); https://doi.org/10.1063/5.0019533
Submitted: 23 June 2020 . Accepted: 19 July 2020 . Published Online: 04 August 2020

Micah S. Haseman, Brenton A. Noesges, Seth Shields, John S. Cetnar, Amber N. Reed, Hayder A. Al-Atabi, James H. Edgar, and Leonard J. Brillson

openaccess

View Online Export Citation CrossMark

additive manufacturing epitaxial crystal growth cerium oxide polishing powder silver nanoparticles sputtering targets III-IV semiconductors CVD precursors europium phosphors
gallium lump glassy carbon nanodispersions InAs wafers laser crystals ultra high purity materials MOFs
surface functionalized nanoparticles rare earth metals photovoltaics refractory metals MOCVD
organometallics quantum dots superconductors transparent ceramics ultra high purity silicon
deposition slugs OLED Lighting spintronics solar energy
osmium nanoribbons thin films chalcogenides AuNPs
GDC li-ion battery electrolytes 99.999% ruthenium spheres
endohedral fullerenes copper nanoparticles diamond micropowder
CIGS MBE grade materials palladium catalysts flexible electronics perovskite crystals yttrium iron garnet alternative energy h-BN
beta-barium borate borosilicate glass dysprosium pellets YBCO gold nanocubes graphene oxide macromolecules photonics
pyrolitic graphite 3d graphene foam indium tin oxide mesoporus silica rhodium sponge fiber optics beamsplitters infrared dyes zeolites
raman substrates sapphire windows tungsten carbide InGaAs fused quartz metallocenes platinum ink buckyballs Ti-6Al-4V
barium fluoride carbon nanotubes lithium niobate scandium powder

AMERICAN ELEMENTS
THE ADVANCED MATERIALS MANUFACTURER®

American Elements opens up a world of possibilities so you can **Now Invent!**

Over 15,000 certified high purity laboratory chemicals, metals, & advanced materials and a state-of-the-art Research Center. Printable GHS-compliant Safety Data Sheets. Thousands of new products. And much more. All on a secure multi-language "Mobile Responsive" platform.

Now Invent.™
The Next Generation of Material Science Catalogs
www.americanelements.com

© 2020 Author(s).

Cathodoluminescence and x-ray photoelectron spectroscopy of ScN: Dopant, defects, and band structure

Cite as: APL Mater. 8, 081103 (2020); doi: 10.1063/5.0019533
Submitted: 23 June 2020 • Accepted: 19 July 2020 •
Published Online: 4 August 2020

View Online Export Citation CrossMark

Micah S. Haseman,[1,a] Brenton A. Noesges,[1] Seth Shields,[1] John S. Cetnar,[2] Amber N. Reed,[3] Hayder A. Al-Atabi,[4,5] James H. Edgar,[4] and Leonard J. Brillson[1,6]

AFFILIATIONS

[1]Department of Physics, The Ohio State University, Columbus, Ohio 43210, USA
[2]Air Force Research Laboratory, Sensors Directorate, Wright Patterson AFB, Ohio 45433, USA
[3]Air Force Research Laboratory, Materials and Manufacturing Directorate, Wright Patterson AFB, Ohio 45433, USA
[4]Tim Taylor Department of Chemical Engineering, Kansas State University, Manhattan, Kansas 66506, USA
[5]Chemical Engineering Department, The University of Technology, Baghdad, Iraq
[6]Department of Electrical and Computer Engineering, The Ohio State University, Columbus, Ohio 43210, USA

[a]**Author to whom correspondence should be addressed:** haseman.2@osu.edu

ABSTRACT

We have studied the optical band and defect transitions of ScN, a group IIIB transition metal nitride semiconductor with electronic and optoelectronic applications. Recent works have focused on the degenerate nature of ScN by substitutional impurities O_N and F_N, which shift the direct (X–X) gap transition to higher energies via the Burstein–Moss effect. We used cathodoluminescence spectroscopy (CLS) to observe optical signatures of both the midgap V_N precursor to O_N doping as well as above the direct (X–X) bandgap corresponding to band-to-band transitions from four separate conduction bands near the Γ point with the valence band minimum, in agreement with the calculated band structure diagrams. Thin film ScN grown by reactive magnetron sputtering displays mild degenerate doping by substitutional oxygen as indicated by elevated (X–X) transition energies and the presence of Sc–O bonding determined via x-ray photoelectron spectroscopy (XPS), while ScN grown by physical vapor transport exhibited the intrinsic, non-degenerate (X–X) bandgap predicted by theory. CLS reveals a sharp, sub-bandgap emission at 1.26 eV for sputter grown ScN on GaN, which we attribute to nitrogen vacancies (V_N) based on surface sensitive CLS and XPS chemical trends. This finding is in strong agreement with theoretical calculations for V_N predicting the formation of a defect energy level within the gap.

© 2020 Author(s). All article content, except where otherwise noted, is licensed under a Creative Commons Attribution (CC BY) license (http://creativecommons.org/licenses/by/4.0/). https://doi.org/10.1063/5.0019533

The rocksalt-structure semiconductor ScN is a relatively unexplored transition metal nitride with outstanding physical properties that, combined with its III-nitride counterparts, has the potential to dramatically expand the range of their electrical, optical, and thermoelectric device applications.[1–3] With its small lattice constant mismatch with GaN (<1%) and relatively small bandgap, ScN can in principle provide a viable substitute for InN in nitride heterostructures.[4] Together with its relatively high electron mobility at high carrier densities, the ability to grow bulk crystals, and its high melting point (>2600 °C), ScN is envisioned as a potential buffer, interface layer, heterojunction, or alloy with GaN and other nitrides for new optoelectronic, piezoelectronic, spintronic, or thermoelectric applications.[4–8] Fabrication of bulk and thin film ScN by using both chemical and physical vapor techniques makes it an attractive material for the integration with current nitride semiconductor systems.[4,9–15]

ScN has an indirect bandgap (Γ–X) calculated to be between 0.9 eV and 1.3 eV, although this gap is not often evident in

© Author(s) 2020

typical spectroscopies due to the relatively small cross section of the (Γ–X) transition.[13,14,16,17] Instead, the (X–X) direct gap transition E_g (X–X), calculated as ~2.0 eV via density functional theory (DFT), is detected between 2 eV and 3.2 eV experimentally.[14,18,19] Only one spectroscopic observation of a (Γ–Γ) transition has been reported with $E_{g(\Gamma-\Gamma)} \approx 4.25$ eV.[12] The experimental deviations in the (X–X) transition are attributed to unintentional degenerate doping, which pushes the Fermi level into the conduction band, effectively increasing E_g(X–X) beyond its intrinsic value due to the Burstein–Moss effect.[20] Substitutional oxygen in nitrogen sites (O_N) is a primary source of this background doping.[21–23] Recent theoretical calculations have shown that O_N is thermodynamically stable across the gap[24] and that ScN films are subject to oxidation even after deposition.[19] Nayak *et al.*[21] recently reported on the rigidity of the ScN band structure with respect to O_N and Mg on Sc sites (Mg_{Sc}), while effectively tuning the material from *n*- to *p*-type and confirming that while O_N contributes excess electrons to the conduction band, neither impurity introduces defect states within the fundamental bandgap. In the same paper, they note that V_N introduces a sharp peak in the density of states just above the valence band edge when ionic relaxation is considered. This agrees with recent calculations confirming that nitrogen vacancies (V_N) are stable for Fermi level positions across the gap with a low energy of formation in Sc-rich environments,[24] and that V_N is the only stable native point defect expected to produce a transition level within the gap.[22,24,25] Moreover, as anionic vacancies, V_N have the potential to generate a large number of carriers that could contribute to the unintentional background doping in ScN.[3]

In contrast to considerable theoretical studies of the ScN band structure, direct measurements of its bulk bandgap energies are relatively unexplored. Furthermore, the electrical properties of gap states in ScN are relevant to its use in coupling light and electrons since such states can either increase or decrease free carrier density. While native defect vacancies are predicted to introduce states within the ScN bandgap,[22,24,25] experimental measurements have not yet been available. Instead, oxygen atoms substituting for nitrogen in V_N sites, e.g., O_N, provide excess electrons the conduction band E_C, raising E_F above E_C[18] and increasing the effective optical bandgap due to the Burstein–Moss effect.[20] ScN has a strong affinity for oxygen since Sc forms an oxide, Sc_2O_3, that is much more stable than ScN ($\Delta H_f^0 = -1908.3$ kJ/mol vs −313.8 kJ/mol, respectively).[26] In order to measure and identify the physical nature of gap states in ScN together with the role they can play in doping, we used depth-resolved cathodoluminescence spectroscopy (DRCLS) to measure all the lowest ScN direct bandgaps up to 5 eV, the deep level defect believed central to increasing free carrier density, and the effect of local ScN off-stoichiometry. Because of the direct connection between direct bandgap luminescence and carrier density,[18] together with the ability to measure the electronic features from extremely thin overlayers, DRCLS can measure variations in defects and doping density both laterally and in depth. Coupled with surface science techniques, it can correlate defect densities and their spatial distribution to determine how these defects depend on local ScN stoichiometry. In this way, DRCLS provides clear experimental measurement of all the ScN energy band separations up to 5 eV above the valence band, not only confirming current theory predictions, in general, but also providing specific band energies to compare with more refined calculations in the future. Furthermore, the combination of the near-surface sensitive cathodoluminescence and x-ray photoemission spectroscopies establishes the optical signature for the nitrogen vacancy in ScN, O substitution into which creates the shallow donor level responsible for degenerate doping. Optical identification of this doping precursor, V_N, can help to understand growth and processing that influence ScN doping.

In this work, we probe the electronic structure of ScN films grown by reactive magnetron sputtering and physical vapor transport (PVT) by DRCLS. The sputter grown ScN films have (X–X) direct gaps above the theoretically predicted intrinsic value due to unintentional degenerate background doping that shifts the transition to higher energies in accordance with the Burstein–Moss effect. On the other hand, DRCL spectra show that ScN grown by PVT exhibits the intrinsic (X–X) direct bandgap at 1.98 eV as predicted by density functional theory. Four optical signatures above the (X–X) direct gap, common to all samples, reflect the ScN band structure and are attributed to transitions to the valence band from four overlapping conduction bands near the Γ point as outlined in the calculated ScN band structure diagram. Additionally, there is a unique infrared (IR) emission at 1.26 eV for sputter grown ScN on GaN. The origin of this feature was investigated by a unique combination of x-ray photoemission spectroscopy (XPS) with surface sensitive cathodoluminescence spectroscopy (CLS) to correlate chemical trends with variations in spectral intensity, a technique that was recently used to investigate a related nitride system.[27] We attribute the 1.26 eV luminescence to nitrogen vacancies (V_N) based on [Sc]:[N] chemical trends and a close agreement with density functional theory (DFT) calculations for V_N predicting the formation of a defect energy level within the bandgap.

ScN thin films, with thicknesses less than 100 nm, were grown by reactive magnetron sputtering in an ultra-high vacuum system with base pressures less than 10^{-6} Pa (10^{-8} Torr). The ScN films were grown on (001)-MgO and (0001)-Fe-doped GaN at growth temperatures of 550 °C and 760 °C, respectively, with 2.67 Pa (20 mTorr) of argon and nitrogen. The N_2 to Ar ratio was 0.75 for both films. Previous experiments had shown that these conditions resulted in highly oriented crystalline ScN.[22] A 5 μm-thick ScN layer was grown by PVT on a single crystal (100) oriented tungsten substrate as described in Ref. 10.

We carried out DRCLS using a glancing incidence electron gun in an ultrahigh vacuum (UHV) chamber with a CaF_2 focusing lens mounted inside the chamber coupled to a fiber optic cable outside the chamber connected to an Oriel monochromator and a thermoelectric cooled CCD detector. The incident electron beam generates a cascade of secondary electrons with energies sufficient for the excitation of valence electrons into the lowest conduction bands as well as into the higher lying unoccupied electronic bands, providing numerous pathways for radiative recombination. The excitation depth of the incident electron beam is tunable via accelerating voltage while variable deflecting potentials allow for beam positioning, providing both depth and spatial resolution.[28–30] XPS was performed using a PHI VersaProbe 5000^{TM} system equipped with a scanning XPS microprobe x-ray source with Al Kα hυ = 1486.6 eV, full-width at half-maximum ≤0.5 eV, and hemispherical energy analyzer with a pass energy of 23.5 eV and 0.05 eV step. Photoelectrons were collected at a takeoff angle of 45°. The XPS system is equipped with a two-stage sample surface neutralization system consisting of a 10 eV

© Author(s) 2020

electron flood gun and 10 eV Ar^+ ion beam to minimize the charging effects at the sample surface. Chemical composition and relative atomic ratios were determined using the PHI MultiPak analysis suite using a Shirley baseline and relative sensitivity factors of 36.389, 8.405, 12.863, and 5.108 for Sc 2*p*, N 1*s*, O 1*s*, and C 1*s*, respectively.[31] Additional curve fitting was performed using a Shirley baseline with Voigt line shapes.

Figure 1 presents cathodoluminescence spectra for ScN grown by magnetron sputtering on Fe:GaN and MgO and ScN grown by PVT on tungsten. All the three samples have common energy transitions above E_g(X–X) that vary significantly in intensity but are consistent in energy at ~3.0 eV, 3.5 eV, 4.0 eV, and 4.6 eV. The 5.1 eV peak could be considered a fifth common feature, but its energy is less certain due to the equipment-related uncertainties in the deconvolved peak positions. To our knowledge, only one other study reports an optical transition above (X–X). Those optical absorption measurements attributed a 4.25 eV feature to the direct (Γ–Γ) transition.[12] In contrast, the four unique higher energy optical signatures we identify here exhibit energies that are independent of growth methods and growth parameters and are, thus, likely to reflect the ScN bulk band structure.

Figure 2 presents an example of the calculated ScN band structure obtained using density functional calculations with the HSE06 hybrid exchange correlation functional showing the indirect (Γ–X) bandgap at 0.9 eV and the direct (X–X) transition at 2.02 eV.[18] In addition, there are two degenerate conduction bands at the Γ point that split into four separate bands labeled 1–4 that span ~2 eV. A similar conduction band behavior is depicted in the band structure calculations of Refs. 17 and 24. As described above, the incident electron beam in CLS generates a cascade of secondary electrons that can excite valence electrons into higher lying conduction bands. Here, electrons promoted to the multiple, separate conduction bands recombine with holes in the valence band near the Γ point and give rise to the four distinct optical signatures shown in Fig. 1, which are separated by ~0.5 eV. The lowest fundamental (Γ–Γ) transition for the band structure in Fig. 2 is 3.75 eV; however, this energy is extremely sensitive to DFT specifics, varying anywhere from 2.4 eV to 4.49 eV.[17,18] Future theoretical works could expand on the reported band structure calculations to confirm the expected transition energies from these four conduction bands.

Both sputter-grown ScN films exhibit E_g(X–X) transition energies above the intrinsic value of 2.0 eV. The E_g(X–X) peak for ScN on Fe:GaN is centered at 2.16 eV, while the peak center for ScN on MgO is at 2.21 eV. These elevated energies are a result of the Burstein–Moss effect[20] and the unintentional degenerate background doping that moves the Fermi level into the conduction band. For the ScN film grown on MgO, the measured value of E_g(X–X) is location dependent and varies between 2.06 eV and 2.21 eV as shown in the supplementary material, Fig. S1. This inhomogeneity is not observed for ScN on Fe:GaN and may be due to the better lattice match between ScN and GaN compared to ScN and MgO. Variations in the measured (X–X) transition energies are reflective of inhomogeneities in degenerate doping concentrations. It is, therefore, important to ensure that spectroscopic and absorption measurements of the ScN direct bandgap (X–X) be performed cautiously, taking into consideration the geometry of the measurement region and any potential spatial variations. Comparison of the optical gap values in Figs. 1(a) and 1(b) with those of Ref. 18 suggests carrier concentrations on the order of 1–2 × 10^{20} cm^{-3}, which is comparable to those for sputter-grown ScN on MgO of ~4 × 10^{20} cm^{-3} as determined by Hall effect measurements.[22] For ScN grown by PVT, the (X–X) transition energy is 1.98 eV as shown in Fig. 1(c). This is, to our knowledge, the lowest experimental value reported to date and is in agreement with the calculated values for the intrinsic (X–X) bandgap of 2.02 eV[18] and 1.98 eV,[24] implying non-degenerate levels of background doping by substitutional oxygen or other donor species. A previous study of the PVT-grown ScN exhibited significantly higher carrier densities from temperature-dependent Hall effect measurements.[32] The significant variation between two such PVT-grown ScN samples may depend on differences in growth conditions or even inhomogeneities within the same sample as evidenced by the orders-of-magnitude variation in carrier density at a single sputtered ScN surface corresponding to the spectral features in Fig. S1.

For the ScN sample grown on Fe:GaN, there is an additional CL feature in the infrared (IR) at 1.26 eV; the onset of that can be seen in Fig. 1(a), and the full spectrum is shown in Fig. 3. To resolve the

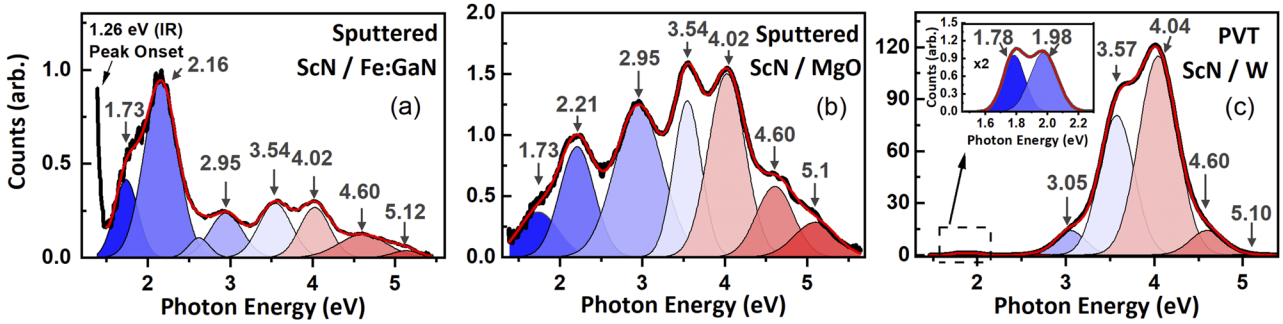

FIG. 1. Cathodoluminescence spectra for ScN films grown by reactive magnetron sputtering [(a) and (b)] and physical vapor transport (c). The inset in panel (c) shows the spectral features from 1.4 eV–2.3 eV. (X–X) transition energies vary from 2.16 eV to 2.21 eV for the sputter-grown films and are at the intrinsic value of 1.98 eV for the PVT-grown film. The transitions above the (X–X) direct gap are common to all films and are consistent in energy across different growth methods and substrate types. All spectra are normalized by (X–X) NBE emission.

© Author(s) 2020

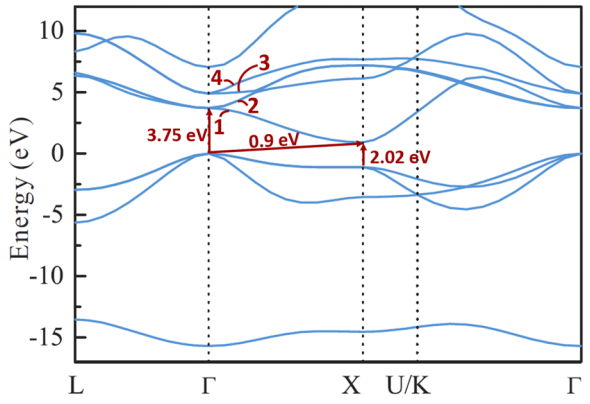

FIG. 2. Energy bands and bandgap transitions corresponding to the features in Fig. 1 indicated in the DFT-calculated ScN band structure along high-symmetry directions in the Brillouin zone. Reproduced with permission from Deng *et al.*, Phys. Rev. B **91**, 045104 (2015). Copyright 2015 American Physical Society.

1.26 eV feature shown in Fig. 3, we rotated the diffraction grating to increase the IR detection efficiency and to project a smaller range of energies on the CCD array, which improved the energy resolution and better resolved the evenly spaced $\Delta E = 75$ meV ripples between 1.5 eV and 2.1 eV below the (X–X) transition. This energy is in relatively good agreement with theoretical calculations for longitudinal optical phonons (71 meV) and experimentally observed Raman spectral peak shifts (73 meV) for LO(X).[33] It is unlikely that these ripples are experimental artifacts as they exhibit both a position and specimen dependence and appear only for the ScN film deposited on

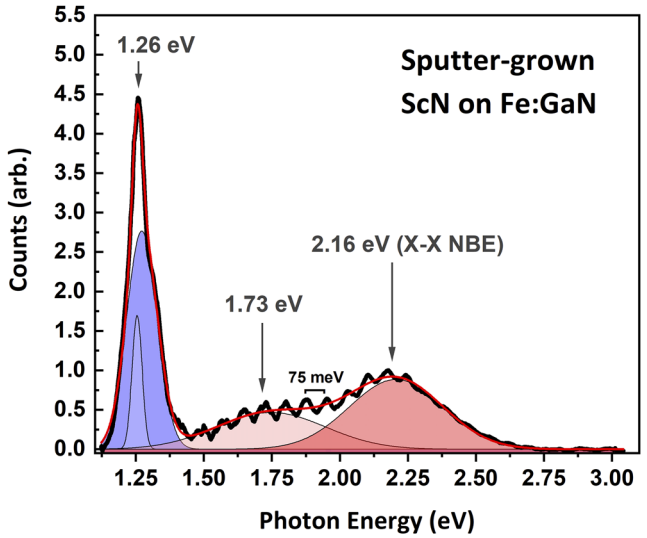

FIG. 3. Cathodoluminescence spectrum for ScN on Fe:GaN from 1.1 eV–3.0 eV showing the IR emission at 1.26 eV in relation to the ScN (X–X) bandgap at 2.16 eV. The periodic ripples spaced at 75 meV correspond to ScN longitudinal optical phonon modes predicted theoretically at 71 meV and observed via Raman spectral peak shift at 73 meV.[33]

Fe:GaN. It is possible, however, that these ripples are due to phonon vibrations associated with a specific defect or impurity such as V_N or O_N, since the ripples appear coupled to the 1.26 eV emission, which we ascribe below to V_N. Additionally, Figs. 1 and 3 reveal a second peak near the (X–X) transition common to all films around 1.73 eV, similar to the peak reported by Saha *et al.*[13] via absorption spectroscopy. They attribute this peak to transitions near the X point based on the band structure diagrams revealing a relatively constant energy difference ($E_c - E_v$) of 1.75 eV when moving from X toward Γ, which leads to a large probability for inter-band transitions based on the high joint densities of states near these regions in the Brillouin zone.

We measured the chemical composition across the surface of 60 nm ScN on Fe:GaN at four different locations as shown schematically in Fig. 4(a) to track the spatial inhomogeneity of Sc and N concentrations and the amount of O incorporated at the surface and bonded to Sc. Representative Sc 2*p* and N 1*s* region scans are shown in Figs. 4(b) and O 1*s* regions in Fig. 4(c). The survey and C 1*s* region scans are shown in the supplementary material, Fig. S2. The C 1*s* peak matched the expected 284.8 eV binding energy and no peak corrections were necessary. Distinct peak splitting/shift toward higher binding energy appears in the Sc 2*p* region due to the presence of both Sc–N and Sc–O bonds, which is consistent with the asymmetry of the O 1*s* region and the small shoulder shifted toward lower binding energy (more electron withdrawal from Sc). The prevalence of the Sc–O bonds is not surprising, given the extremely high affinity of Sc for O and low energy of formation for oxygen impurities.[24] Similar chemical analysis by More-Chevalier *et al.*[19] for ScN grown on oxide substrates reveals high oxygen concentrations both before and after exposure to air. Their *in situ* XPS measurements show that background oxygen concentrations can be as high as 4% for films grown at 700 °C despite the ultrahigh vacuum environment. This is related to the surface adatom mobility and the suppression of surface roughness, which inhibits oxygen incorporation, although deposition temperatures above 850 °C are necessary to achieve oxygen content below 1 at. %.[34] Here, the presence of Sc–O bonds in high abundance suggests that oxygen incorporation is responsible for the degenerate background doping, and the shift in the optical (X–X) bandgap to 2.16 eV due to the Burstein–Moss effect. Similarly, for the ScN film grown on MgO with a (X–X) bandgap of 2.2 eV [Fig. 1(b)], Cetnar *et al.*[22] showed via secondary ion mass spectroscopy (SIMS) that O_N impurities were responsible for the degenerate background doping and high carrier concentrations around 5×10^{20} cm^{-3}.

At the same four locations that we acquired XPS, we used low voltage ($E_b = 0.5$ kV) CLS to probe 5 nm–8 nm below the ScN free surface as indicated by Monte Carlo simulations for electron–hole pair generation shown in the supplementary material, Fig. S3. Each of the spectra was deconvolved to obtain the fitted peak area ratios to track changes in the 1.26 eV emission relative to the (X–X) direct bandgap emission. Two diffraction grating positions were used to acquire the ScN emission spectrum in its entirety. Position 1 provided energies from 1.5 eV to 5.6 eV as in Fig. 1, while position 2 extended the range in the IR with energies from 1.1 eV to 3.0 eV as in Fig. 3. Figures 5(a) and 5(b) display CL spectra for locations 1 and 4, which represent the least and most intense IR emission, respectively. The spectra at each location and at each grating position were normalized by the (X–X) bandgap emission. The relative atomic ratios

© Author(s) 2020

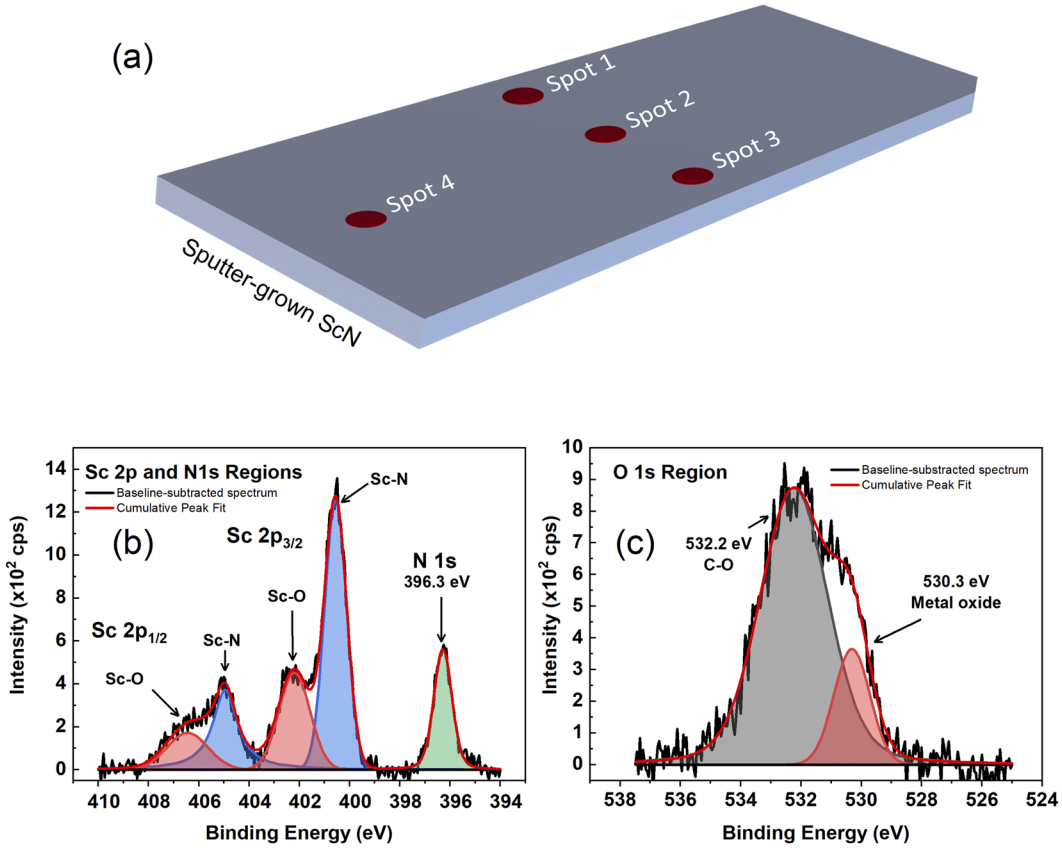

FIG. 4. (a) Diagram of 60 nm sputtered ScN showing the four measurement locations. (b) Sc 2p and N 1s region scan showing multiple peaks for Sc–O and Sc–N bonds. A common baseline was used to fit the Sc 2p and N 1s regions simultaneously. (c) O 1s region scan showing the C–O bond and small shoulder to be shifted to lower binding energy indicating Sc–O bonding. All XPS region scans are shown with a subtracted Shirley baseline.

[N]:[Sc] are shown alongside for comparison of spectral intensities with stoichiometry. The intensity of the 1.26 eV emission normalized to the (X–X) bandgap luminescence across the sample surface varies with position. Figure 5(c) shows the deconvolved peak areas of the 1.26 eV emission normalized by the (X–X) peak area as a function of total Sc to N atomic ratios. From this, we see that regions with lower N/Sc ratios have more intense 1.26 eV luminescence. Based on the thermodynamic energy stability of V_N, the 1.26 eV luminescence is likely due to radiative recombination with defect levels within the bandgap introduced by nitrogen vacancies. The absence of any 1.26 eV emission for the ScN film grown on the MgO substrate can be attributed to the high stability of the MgO substrate at a relatively low deposition temperature, which inhibits the formation of a blocking layer that would otherwise prevent oxygen migration across the film/substrate interface. Atomic oxygen is very mobile and readily diffuses across interfacial boundaries, affecting the optical and electrical properties in oxide films.[35,36] Here, the migration of oxygen into the nitride thin film is thermodynamically driven by the extremely high affinity of Sc and O and the low formation energy of O_N. This is evident in the SIMS analysis of the sputtered ScN film on MgO showing the outdiffusion of O from the MgO substrate.[22]

The direct detection of vacancies and vacancy complexes in materials is not possible by standard chemical analysis techniques like XPS and SIMS. In Fig. 5(c), the 1.26 eV luminescence intensity shifts abruptly as [Sc]:[N] changes from 1.38 to 1.41, which is unusual considering the smaller relative change in luminescence as [Sc]:[N] varies from 1.41 to 1.53. Here, V_N concentrations are indirectly inferred via cation/anion stoichiometries, which are reflective of total Sc vs N and do not differentiate between amounts of Sc bonded to N and Sc bonded to O. In the case of ScN, standard chemical analysis via XPS is inhibited by the high background concentration of oxygen both on the surface and within the lattice, which forms scandium oxide (ScO_x) bonds as well as both oxynitride (ScO_xN_y) and hydroxide (ScO_xH_y) bonds. This mixture of chemical bonds and binding energies leads to a broadening of the photoelectron kinetic energies and to core level spectra that can be reasonably fit with or without distinguishing of the oxynitride and hydroxide peaks. Argon sputtering can remove the surface carbon and surface oxide layers; however, it may introduce sub-stoichiometric regions

© Author(s) 2020

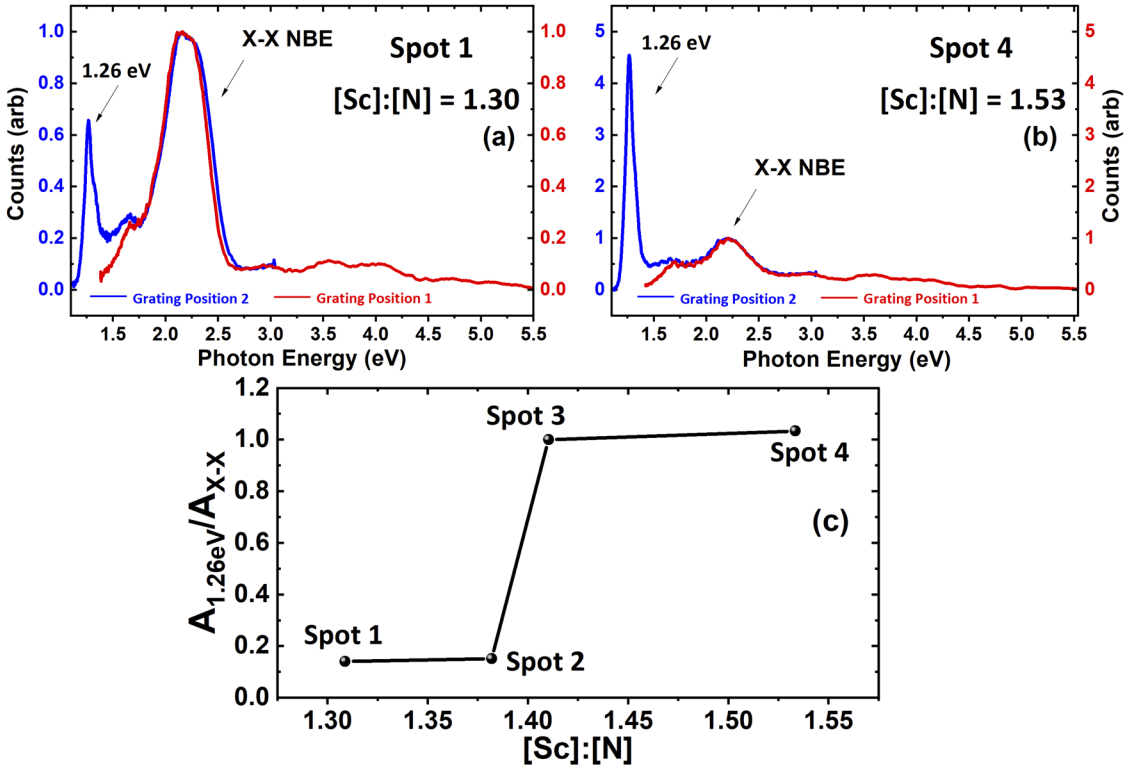

FIG. 5. CL surface spectra (E_b = 0.5 keV) for different ScN regions showing the least intense (a) and most intense (b) 1.26 eV emission with respect to the (X–X) direct bandgap. (c) Deconvolved CL peak area ratios comparing the relative intensity of the 1.26 eV feature with [Sc]:[N] atomic ratios acquired by XPS.

(ScN_x) of ScN[34] and broadens the Sc 2*p* and N 1*s* regions, affecting the baseline fitting and enhancing Sc 2*p* satellite features.[19] Thus, the separation of the appropriate ScO_x, ScO_xN_y, and ScO_xH_y bonds leads to inherent ambiguities in fitting the Sc 2*p* region, while the comparison of total Sc to N content minimizes the margin of error. Consequently, the [Sc]:[N] atomic ratios presented in Fig. 5(c) do not explicitly account for the amount of Sc–O vs Sc–N bonding, which could affect the total V_N concentrations. For example, an increased ratio of Sc–O to Sc–N bonds in a region with a high [Sc]:[N] ratio would suggest substitutional oxygen atoms on nitrogen sites and a reduction of nitrogen vacancies despite the high V_N concentration inferred by the atomic Sc/N ratio. However, the variable intensity of the 1.26 eV emission as a function of [Sc]:[N] ratios in Fig. 5(c) is in strong agreement with theoretical calculations for V_N predicting the formation of a defect energy level within the bandgap. In Sc-rich environments, V_N has a negative energy of formation that is stable across the gap.[24] Under both Sc- and N-rich conditions, V_N has an energy of formation lower than any other native point defect,[22,24] the one exception being substitutional oxygen, which we include as a native species based on its prevalence and significance in electrical transport. However, the presence of O_N does not affect the ScN electronic band structure, and no new defect levels are introduced within the gap that could provide radiative pathways.[21] Moreover, theoretical calculations have shown that nitrogen vacancies are expected to introduce a defect energy level within the ScN bandgap with a high density of states.[21,24,25] Similarly, the heat of formation energies vs Fermi level calculations suggest a V_N charge state transition ~1 eV above the VBM at the Γ point,[24] which is in reasonable agreement with the absorption thresholds in the range of 1.2 eV–1.4 eV in spectroscopic ellipsometry and transmission/reflectivity measurements.[16] Alternatively, the reduction of the nominal Sc^{3+} charge state to Sc^{2+} by donor electrons from nearby V_N could lead to sharp transitions in the infrared similar to the Ti^4 to Ti^{3+} transition in $SrTiO_3$ due to nearby V_O.[37] In either case, the 1.26 eV emission is likely due to the electronic recombination with nitrogen vacancies, although defect energy levels due to possible trace impurities beyond our threshold of detection cannot be ruled out.

In summary, we used CLS to probe the ScN band structure, revealing multiple higher energy optical signatures, above the ScN direct (X–X) bandgap that are consistent across growth methods and that correspond to transitions from four individual conduction bands near the Γ point, which are in agreement with the calculated ScN band structure diagrams. Additionally, CLS of sputter-grown ScN reveals direct (X–X) transitions that are shifted to higher energies, which reflect Fermi level positions elevated by unintentional degenerate *n*-type doping. In contrast, the (X–X) transition for PVT-grown ScN is at the intrinsic calculated value of 1.98 eV.

© Author(s) 2020

Sub-bandgap luminescence at 1.26 eV is observed for sputter-grown ScN on Fe:GaN that varies in intensity with [Sc]:[N] atomic ratios measured via XPS. We attribute this emission to nitrogen vacancies (V_N) based on spectral intensities observed with surface sensitive CLS and XPS chemical trends for relative [N] concentrations. This finding agrees with theoretical calculations predicting a V_N defect energy level with a high density of states ~1 eV above the Γ point VBM as well as experimental absorption onsets between 1.2 eV and 1.4 eV. Since O substitution into V_N defects creates the shallow donor level responsible for degenerate doping, optical identification of this doping precursor can help understand the growth and processing that influence ScN doping.

See the supplementary material for cathodoluminescence of ScN on MgO showing the spatial variation of the (X–X) direct bandgap energy, Monte Carlo simulations for e–h excitation depth of ScN, and x-ray photoelectron survey and C 1*s* region scans for ScN on Fe:GaN.

L.J.B., M.S.H., and S.S. acknowledge the support from the National Science Foundation, Grant No. DMR 18-00130. A.H. and J.H.E. acknowledge the support for ScN crystal growth from the National Science Foundation under Grant No. DMR-1508172. This research was also supported by the Air Force Office of Scientific Research through Project No. FA9550-RY17COR490 (J.S.C. and A.N.R.).

DATA AVAILABILITY

The data that support the findings of this study are available within the article and the supplementary material.

REFERENCES

[1] B. Saha, T. D. Sands, and U. V. Waghmare, J. Phys.: Condens. Matter **24**, 415303 (2012).
[2] A. Shakouri, Annu. Rev. Mater. Res. **41**, 399 (2011).
[3] B. Biswas and B. Saha, Phys. Rev. Mater. **3**, 020301 (2019).
[4] S. W. King, R. F. Davis, and R. J. Nemanich, J. Vac. Sci. Technol., A **32**, 061504 (2014).
[5] L. Lupina, M. H. Zoellner, T. Niermann, B. Dietrich, G. Capellini, S. B. Thapa, M. Haeberlen, M. Lehmann, P. Storck, and T. Schroeder, Appl. Phys. Lett. **107**, 201907 (2015).
[6] M. A. Moram, M. J. Kappers, and C. J. Humphreys, Phys. Status Solidi C **7**, 1778 (2010).
[7] A. Herwadkar and W. R. L. Lambrecht, Phys. Rev. B **72**, 235207 (2005).
[8] J. Missaoui, I. Hamdi, and N. Meskini, J. Magn. Magn. Mater. **413**, 19 (2016).
[9] J. H. Edgar, T. Bohnen, and P. R. Hageman, J. Cryst. Growth **310**, 1075 (2008).
[10] H. A. Al-Atabi, N. Khan, E. Nour, J. Mondoux, Y. Zhang, and J. H. Edgar, Appl. Phys. Lett. **113**, 122106 (2018).
[11] Z. Gu, J. H. Edgar, J. Pomeroy, M. Kuball, and D. W. Coffey, J. Mater. Sci.: Mater. Electron. **15**, 555 (2004).
[12] J. More-Chevalier, S. Cichoň, J. Bulíř, M. Poupon, P. Hubík, L. Fekete, and J. Lančok, AIP Adv. **9**, 015317 (2019).
[13] B. Saha, G. Naik, V. P. Drachev, A. Boltasseva, E. E. Marinero, and T. D. Sands, J. Appl. Phys. **114**, 063519 (2013).
[14] T. Ohgaki, K. Watanabe, Y. Adachi, I. Sakaguchi, S. Hishita, N. Ohashi, and H. Haneda, J. Appl. Phys. **114**, 093704 (2013).
[15] M. A. Moram, T. B. Joyce, P. R. Chalker, Z. H. Barber, and C. J. Humphreys, Appl. Surf. Sci. **252**, 8385 (2006).
[16] D. Gall, M. Städele, K. Järrendahl, I. Petrov, P. Desjardins, R. T. Haasch, T.-Y. Lee, and J. E. Greene, Phys. Rev. B **63**, 125119 (2001).
[17] B. Saha, J. Acharya, T. D. Sands, and U. V. Waghmare, J. Appl. Phys. **107**, 033715 (2010).
[18] R. Deng, B. D. Ozsdolay, P. Y. Zheng, S. V. Khare, and D. Gall, Phys. Rev. B **91**, 045104 (2015).
[19] J. More-Chevalier, S. Cichoň, L. Horák, J. Bulíř, P. Hubík, Z. Gedeonová, L. Fekete, M. Poupon, and J. Lančok, Appl. Surf. Sci. **515**, 145968 (2020).
[20] E. Burstein, Phys. Rev. **93**, 632 (1954).
[21] S. Nayak, M. Baral, M. Gupta, J. Singh, M. Garbrecht, T. Ganguli, S. M. Shivaprasad, and B. Saha, Phys. Rev. B **99**, 161117 (2019).
[22] J. S. Cetnar, A. N. Reed, S. C. Badescu, S. Vangala, H. A. Smith, and D. C. Look, Appl. Phys. Lett. **113**, 192104 (2018).
[23] J. Casamento, H. G. Xing, and D. Jena, Phys. Status Solidi B **257**, 1900612 (2020).
[24] Y. Kumagai, N. Tsunoda, and F. Oba, Phys. Rev. Appl. **9**, 034019 (2018).
[25] S. Kerdsongpanya, B. Alling, and P. Eklund, Phys. Rev. B **86**, 195140 (2012).
[26] O. Kubaschewski, C. B. Alcock, and P. J. Spencer, *Materials Thermochemistry* (Pergamon Press, New York, 1993).
[27] M. S. Haseman, M. R. Karim, D. Ramdin, B. A. Noesges, E. Feinberg, B. H. D. Jayatunga, W. R. L. Lambrecht, M. Zhu, J. Hwang, K. Kash, H. Zhao, and L. J. Brillson, J. Appl. Phys. **127**, 135703 (2020).
[28] L. J. Brillson, J. Phys. D: Appl. Phys. **45**, 183001 (2012).
[29] L. J. Brillson, J. Vac. Sci. Technol., B **19**, 1762 (2001).
[30] L. J. Brillson, *Surfaces and Interfaces of Electronic Materials* (Wiley VCH, Weinheim, 2010).
[31] C. D. Wagner, L. E. Davis, M. V. Zeller, J. A. Taylor, R. H. Raymond, and L. H. Gale, Surf. Interface Anal. **3**, 211 (1981).
[32] H. Al-Atabi, Q. Zheng, J. S. Cetnar, D. Look, D. G. Cahill, and J. H. Edgar, Appl. Phys. Lett. **116**, 132103 (2020).
[33] T. R. Paudel and W. R. L. Lambrecht, Phys. Rev. B **79**, 085205 (2009).
[34] A. le Febvrier, N. Tureson, N. Stilkerich, G. Greczynski, and P. Eklund, J. Phys. Appl. Phys. **52**, 035302 (2019).
[35] C. W. Schneider, M. Esposito, I. Marozau, K. Conder, M. Doebeli, Y. Hu, M. Mallepell, A. Wokaun, and T. Lippert, Appl. Phys. Lett. **97**, 192107 (2010).
[36] C. W. Schneider, M. Döbeli, C. Richter, and T. Lippert, Phys. Rev. Mater. **3**, 123401 (2019).
[37] D. Lee, H. Wang, B. A. Noesges, T. J. Asel, J. Pan, J.-W. Lee, Q. Yan, L. J. Brillson, X. Wu, and C.-B. Eom, Phys. Rev. Mater. **2**, 060403 (2018).

© Author(s) 2020